



Assessment of Numerical Method by Experimental Data for Integrated Hypersonic Vehicles

X. Wen, J. Liu, Z. Liu, Z. Xia and L. Jin

College of Aeronautics and Astronautics, National University of Defense Technology, Changsha, 410073, China

†Corresponding Author Email: xwentst@163.com

(Received March 18, 2018; accepted November 3, 2018)

ABSTRACT

This paper addresses the problem of rapid aerodynamic assessment and experimental verification of integrated hypersonic vehicles. Based on the adaptive Cartesian grid system, the aerodynamic performance of the air-breathing hypersonic vehicle is evaluated. Corresponding shrunken experimental model is investigated in FL-28 transient hypersonic wind tunnel. The grid-independent validation confirms the proposed meshing method and optimal grid parameters. The convergent method is used for the aircraft model to calculate several flight conditions in cold state, and the calculated results are compared with the wind tunnel test data. The results show that in order to validate the accurate non-viscous dynamic characteristics of both internal and external flows, it is necessary to locally encrypt the grids of inner flow channel while ensuring the overall grid density of the aircraft. Although the computational time increases after grid encryption, the rapid prediction method of aerodynamic performance meets the requirements for engineering design. Compared with experimental results, there are several shockwave features invisible in the numerical results due to the simplification of solution procedure. The aerodynamic force coefficients obtained by the numerical method are verified by the experimental data and the same numerical method can be used in the conceptual design phase of aerodynamic shapes, which can greatly shorten the development cycle.

Keywords: Aerodynamic characteristics; Internal and external flow integration; Rapid simulation assessment; Wind tunnel test.

NOMENCLATURE

Add	encryption layer	S	cross section area
C_D	aerodynamic drag coefficient	t	time
C_L	aerodynamic lift coefficient	u, v, w	velocities in x, y and z directions
C_{MZ}	pitching moment coefficient	V	volume of cell
C_v	constant volume specific heat ratio	W	conformation tensor
E	internal energy		
Ma	Mach number	α	angle of attack
Max	layout number	ρ	density
n_x, n_y, n_z	components of unit normal in x, y and z directions	\vec{F}	vector of conserved variables
p	local static pressure	\vec{n}	normal vector
R	universal gas constant	\vec{V}	vector of velocity

1. INTRODUCTION

In recent years, the concept of near-space hypersonic vehicles, especially air-breathing hypersonic vehicles (Sziroczak and Smith, 2016) has attracted an increasing attention among international scholars. The coupling between the

fuselage and propulsion system is a key technology for the development of air-breathing hypersonic vehicles. The simulation of the integrated flow characteristics of internal and external flows determines the accuracy of the aerodynamic characteristics of air-breathing aircraft (Lockwood *et al.*, 1999; Yelan, Yang *et al.* 2015 and

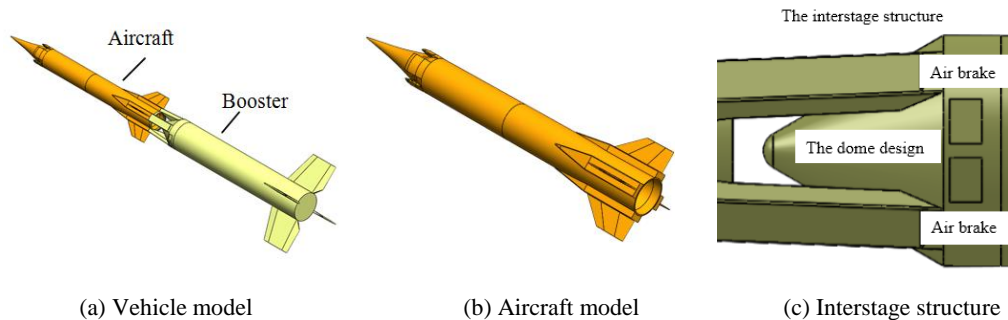


Fig. 1. Geometric shape.

Huang and Wang, 2009). Numerical simulation is the main method used to obtain the aerodynamic characteristics of air-breathing aircraft, and plays a crucial role in the conceptual design stage. Grid generation is the first condition that determines the accuracy of the numerical simulation. Large numbers of aerodynamic configurations need to be calculated in the conceptual design stage of hypersonic vehicles, and quickly obtaining aerodynamic data that possesses a certain degree of accuracy is an important target. Shadloo and Hadjadj (2017) and Sharma *et al.* (2018) studied laminar-to-turbulent transition in the supersonic boundary layer through high-resolution direct numerical simulations, which contributed to hypersonic vehicle development. With the further study of hypersonic vehicles, the aerodynamic shape of the aircraft becomes more and more complex, making grid generation difficult. Therefore, researchers have focused on methods of generating meshes for complex shapes quickly and efficiently (Piscitelli *et al.*, 2017; Dharavath *et al.*, 2016; Rong *et al.*, 2017 & Xu *et al.*, 2017).

Computational meshes are mainly divided into structured meshes and unstructured meshes. Among them, structural meshes are difficult to generate for complex vehicle designs, as they require a great deal of experience and take a great deal of time. There are few studies on the numerical simulation of the aerodynamic properties of internal and external flows using structural meshes in the literature at home and abroad. The use of traditional unstructured grids results in huge numerical simulation with a large number of iterations. Adaptive Cartesian grids are suitable for handling complex aircraft shapes. As a result, the Cartesian grid has been widely used in the concept design of aircraft (Lakshminarayan *et al.*, 2017). However, current applications are mainly aimed at outflow scientific research (Lyu *et al.*, 2017; Xu *et al.*, 2018 & Constant *et al.*, 2017), and there are few studies on integrated air-breathing vehicles. Ashok, Ashok *et al.* (2014) used a Cartesian mesh away from the wall to analyze the chemically-reacting hypersonic laminar flow field both in chemical non-equilibrium flow and thermal equilibrium flow. Yentsch and Gaitonde (2013) proposed that viscous and inviscid simulations yield similar wave structures and that Cartesian grid inviscid simulation identifies specific regions near the side wedges that are important for

defining the shock structure.

In this paper, a full scale hypersonic vehicle with an interstage sluice structure is designed. To obtain the aerodynamic performance fast and promote optimization further, a finite volume solver based on Cartesian grids is adopted to provide the aerodynamic analysis in the conceptual design stage for hypersonic vehicles. Meanwhile, a shrunken experimental model is investigated in wind tunnel and the test data are used to confirm the numerical results.

2. COMPUTATIONAL MODEL AND NUMERICAL METHOD

2.1 Geometry of Hypersonic Vehicles

Due to two sets of geometric models developed by our team, in this paper one with an interstage sluice structure is used for mesh strategy judgment, and the other without booster is occupied for experimental verification. The shape and structure of the models are shown in Fig. 1. More details on the dimensions of the computational models are illuminated in Fig. 2.

2.2 Mesh Generation

On the basis of the vehicle shape and topology, the shell grid was first constructed for whole surfaces according to the uniform grid scale such as a size of 4 mm. The subsequent grid quantity of the vehicle surface is approximately 1.04 million, and 0.6 million for the aircraft surface.

During the generation process, two critical design parameters were advised as key targets relevant to fabrication and identified as “Max” and “Add”. “Max” means the frequency of adjusting scales when the cells are diverged in the entire domain. It is an overall parameter and represents the total multistep cell levels of the variable gradient growth. Besides, “Add” could also decrease the minimum cell scale, as it is surface mesh encryption layer and represents an extra grid encryption level for the closer wall mesh. It means the intensity of minishing the original minimum cell scale. Taking $Max = 9$ and $Add = 2$ as an example, Fig. 3 gives the schematic illustrations of the grid profiles on the longitudinally symmetric plane.

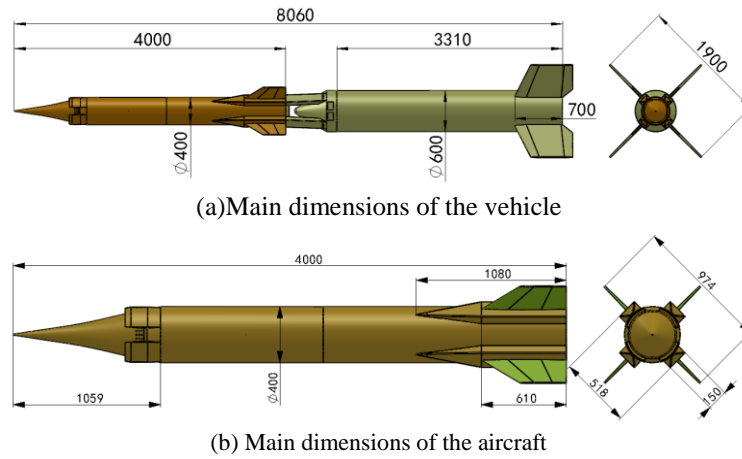


Fig. 2. Dimensions of the computational models.

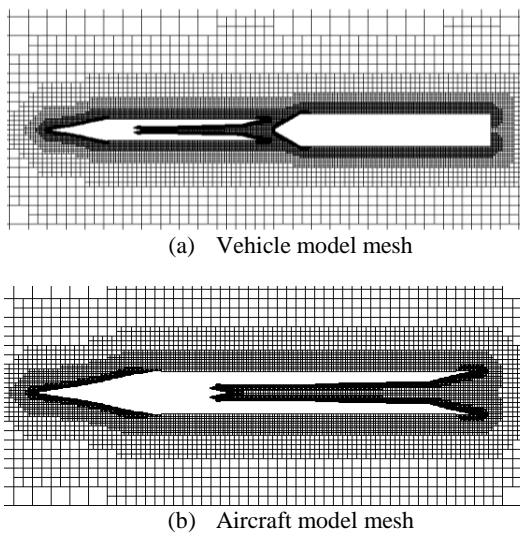


Fig. 3. Comparison of grid profiles on the longitudinal symmetrical plane.

2.3 Computational Methodology

In this study, the compressible Euler equation aerodynamic decomposition integral solver was used to solve the viscosity-free hypersonic flow field for rapid retrieval of a large amount of aerodynamic data for aerodynamic shape design analysis. The solver's governing equation is a three-dimensional, non-viscid, and compressible Euler equation with a complete gas equation as the state equation. The dimensionless equation is described as follows:

$$\iiint_V \frac{\partial W}{\partial t} dV = - \iint_S \vec{F} \cdot \vec{n} dS \quad (1)$$

$$W = \begin{bmatrix} \rho \\ \rho u \\ \rho v \\ \rho w \\ \rho E \end{bmatrix}, \vec{F} \cdot \vec{n} = \begin{bmatrix} \rho \vec{V} \cdot \vec{n} \\ \rho u \vec{V} \cdot \vec{n} + p n_x \\ \rho v \vec{V} \cdot \vec{n} + p n_y \\ \rho w \vec{V} \cdot \vec{n} + p n_z \\ (\rho E + p) \vec{V} \cdot \vec{n} \end{bmatrix} \quad (2)$$

$$E = \frac{C_v p}{\rho R} + \frac{|\vec{V}|^2}{2} \quad (3)$$

Equation (1) has no sticky term, yet it can better reflect the flow field when the viscosity effect is not dominant. The Euler equation does not consider the viscosity, and can greatly improve the computational speed.

Spatial discretization is a cell-based finite volume-type method with first-order upwind values, and the time is discretized with the Runge–Kutta method. The flux vector has a total variation diminishing property because of the use of Minimod limiters. Incoming flow state parameters were adopted as the initial boundary condition. Finally, the simplified physical models were simulated by means of multi-grid acceleration convergence and obtain the desired data rapidly and relatively precisely, which is applied in [Liu *et al.* \(2017\)](#).

3. WIND TUNNEL TEST

The test was conducted in the FL-28 transient hypersonic wind tunnel, which is currently the largest conventional hypersonic wind tunnel that has been put to use in China. The operation mode of the wind tunnel is high-pressure downdraft, vacuum suction, temporary impulse, and electric heating regenerative heater ([Tang *et al.*, 2015](#)). The wind tunnel is mainly used for testing aerodynamic forces, heat, vehicle inter-stage separation characteristics and inlet flow characteristics such as the kind of circular cross air-breathing hypersonic aircraft ([Wang *et al.*, 2015](#)), lifting body integration of hypersonic vehicles ([Jin *et al.*, 2010](#)) and other typical hypersonic vehicles.

As shown in Fig. 4, the FL-28 wind tunnel is mainly contains an air source system, heater system, nozzle, stable section, test section, diffuser, cooler, vacuum system, control system, angle of attack mechanism system, and schlieren system. Working performance indexes, such as the control accuracy of the pressure and the uniformity of the core flow in the test section, all meet the requirements of the

GJB1179-91 quality standard for the flow field in high-speed and low-speed wind tunnels (Wang *et al.*, 2016).

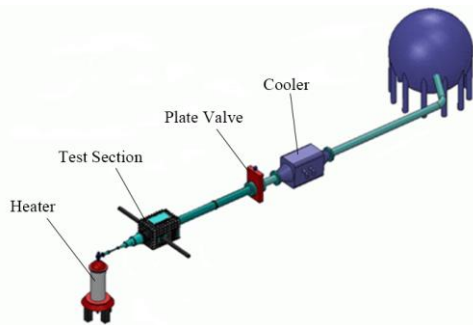


Fig. 4. System composition and layout.

Table 2 Inflow performance in the wind tunnel test

Ma ₀	P _{0t} ,MPa	T _{0t} ,K	P ₀ ,Pa	T ₀ ,K
4	1.0	300	6600	70

The model installation is designed in Fig. 5 and the final installation photo is shown in Fig. 6. The model was installed on the middle bracket of the wind tunnel through the ring balance and supporting struts. Meanwhile, the lip of the model inlet is located within the visual range of the watch window.

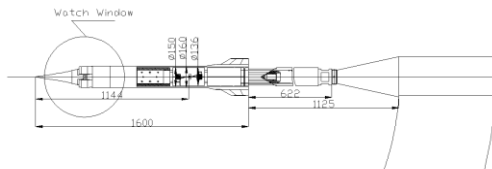


Fig. 5. Installation position diagram (unit:mm).

In the test, the PL4(8)N6-136A ring balance and support rod were used to measure the aerodynamic force and moment of the model. The PPT differential pressure transducer was used to measure the total pressure in the front chamber of the wind tunnel. A $\phi 0.3\text{mm-NiCr-NiSi}$ thermocouple was used to measure the total temperature in the front chamber to calculate the Reynolds number. The voltage signals from the balance and transducer were sampled, amplified, and converted into analog signals by the PRESTON detection system. Finally, the data was calculated and processed by a computer, and the real-time test data and the flow field images were obtained on the computer screen. The inflow performance in the wind tunnel is shown in Table 2. The experimental data were modified as follows. Taking into account the aero-elastic angle of the balance and tail strut, the angle of attack was changed. The effect of the

misalignment between the model torque reference center and balance center was corrected in the torque. Circular interpolation of the total angle of attack carried out to correct base resistance effects.



(a) Front Face



(b) Rear Face

Fig. 6. The model in the hypersonic wind tunnel.

The experimental model has an all-metal structure and scale ratio is 1:2.5. In the experiment, the model adopted the annular tail support method. The model head is made of aluminum while the projectile body is made of steel. The theoretical shape contains a pointed conical head and a columnar projectile body, with four air inlets on the head distributed in 45° cross and the same in the tail of the model to lay out four rudders. The height of the throat is approximately 8 mm and the air inlets have good liquidity. The blockage rate in the FL-28 wind tunnel at zero angle of attack is 0.5%.

4. RESULTS AND DISCUSSION

4.1 Grid Structure Strategy

In order to analyze the impact of the main grid generation parameters on the predicted results, eight grid cases were arranged by controlling the grid space layout parameter *Max* and the vehicle surface mesh encryption layer *Add*; the parameters and estimated results are listed in Table 3. It can be seen that the adjustment of the *Add* parameter caused no significant increase in the amount of grid cells, while increasing *Max* caused the magnitude of the grid cells to increase significantly. Figure 7 and Fig.8 display the effects of the parameters on the.

Table 3 Grid design in domain

Cases	Parameters		Total grid cells, million	Drag Coefficient	Error with Case 8, %	Operation time, hour
	Max	Add				
Case 1	8	1	0.33	0.4167	-5.96	3.1
Case 2	9	0	0.60	0.4063	-8.31	5.7
Case 3	8	2	0.66	0.4425	-0.14	6.1
Case 4	9	1	0.94	0.4502	1.60	8.4
Case 5	8	3	1.50	0.4431	0.02	13.5
Case 6	9	2	1.78	0.4426	-0.11	19.6
Case 7	10	0	2.45	0.4448	0.38	24.4
Case 8	10	1	2.52	0.4431	0.00	25.6

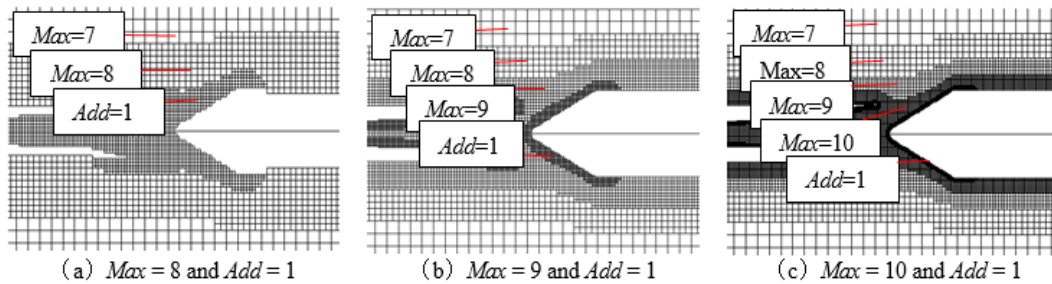


Fig. 7. Illustration of meshes for different Max parameter

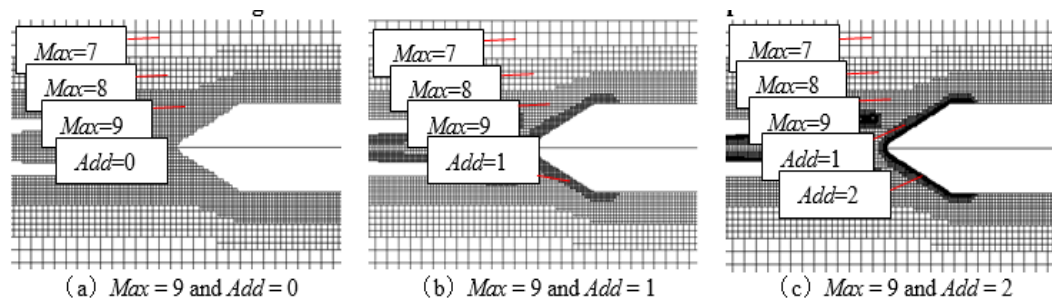


Fig. 8. Illustration of meshes for different Add parameter

local grids, all of which have the same shell mesh with minimum cell size of 4 mm. The computational grid has a significant impact on the aerodynamic forces of the hypersonic vehicle, which is mainly reflected in the structural resolution of the flow field (Aftosmis *et al.*, 1997). Figure 9 shows the pressure contours on the longitudinally symmetric surface of the vehicles. All simulations were performed at zero angle of attack with Ma number of 4.3. In comparison, the inside flow field structures predicted by Case 3 and Case 5 are basically the same, so as to leave out pictures from Case 6 to Case 8. Figure 9 illustrates that the fluid flow through the vehicle surface results in the previous shockwaves appearing at the head cone and more obvious enhanced shockwaves can be seen at the position of the lips, both of which are in accordance with the shockwave interference principle. The inlets capture most flows in the position of internal channels, and the shockwaves are reflected several times in the isolator, which indicates that the inlet starts in cases from Case 3 to Case 8, while the others do not. Then, the shockwaves weaken and disappear gradually from

the combustor or be ahead of the combustor shown as Case 1 and Case 2 to the tail nozzle. However, all of them are followed by a strong bow shockwave at the inter-stage dome.

The predicted drag coefficient converges to a certain value when the grid cells are refined. The drag coefficient obtained by Case 8 is 0.4431 and the difference between Case 3 data is within 0.2%. The results of Case 1 and Case 2 are slightly smaller compared with that of the other cases, and the data of Case 4 is significantly larger than expected. The results of Cases 3, 5, 6, and 8 are in good agreement, but the iteration time shown in Table 3 presents a linearly increasing trend when mesh quantity increased. Considering the error with the results of Case 8, the calculation efficiency and the flow field structures, Case 3 is regarded as the optimal choice among the eight cases. The results show that the Add parameter is more efficient and practical compared with Max under the same grid level, as the efficient cells are in smaller size and occupy more quantities.

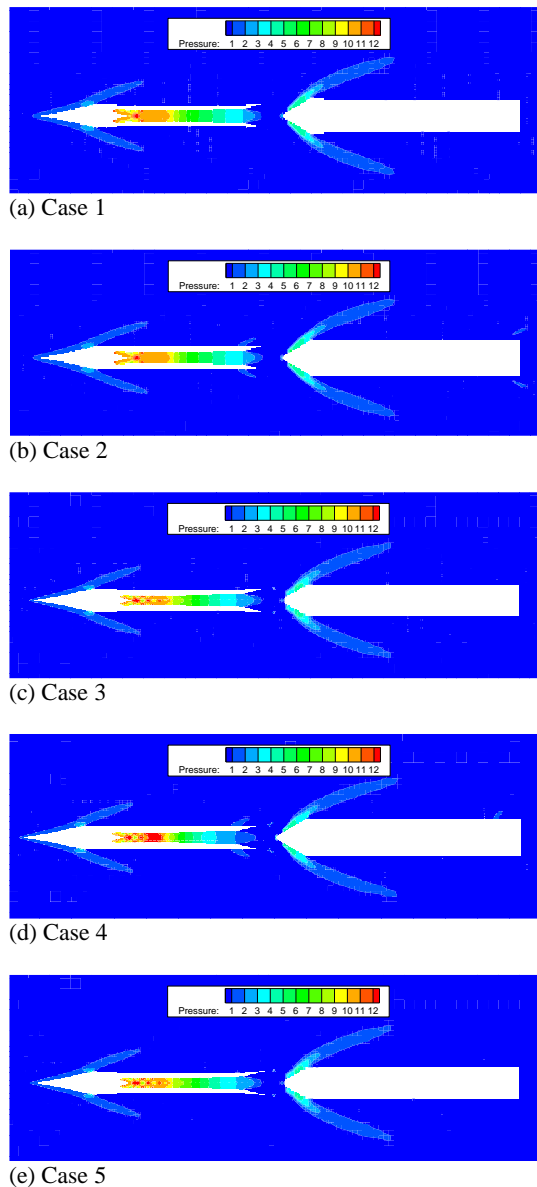


Fig. 9. Pressure contour comparison on the longitudinally symmetric surface.

Therefore, in order to obtain a suitable grid for solving practical problems, the model needs to be repeatedly calculated and compared to develop a grid that can describe the flow field structures and have high computational efficiency. Otherwise, the increase in mesh quantity does not always lead to more accurate aerodynamic results, which is related to the increase in grid size. Where the geometric surface curvature changes sharply, the flow field changes more intensely. Hence, it is necessary to arrange more grid cells in these areas during meshing. In the Cartesian mesh generation process, control surface curvature sensitivity parameter-based Cartesian meshing is used to achieve this requirement. Unlike structured meshes and traditional unstructured meshes, the generation of adaptive Cartesian meshes does not start with the object plane. The surface mesh is only used to characterize the aerodynamic shape of the aircraft. Hence, as long as the surface meshes correctly

represent the geometric shape, the mesh scale is suitable for the iterator.

The rigorous mesh of the aircraft was generated by a convergence scheme called Grid 3, along with Grid 1 and Grid 2 with less cells, and Grid 4 and Grid 5 with more cells. All of them were used to analyze the independence of the aircraft meshes. The numerical simulation conditions selected for the predicted aircraft aerodynamics results shown in Fig. 10 are Ma number of 3, angle of attack of 4° , and sideslip angle of 0° . The curve of the aircraft grid independence verification is presented in Fig. 10. With the increase in grid cells, the aerodynamic coefficients increased at the beginning and then the variations began to emerge gradually. The results are relatively invariant with mesh resolution called Grid 3. The grids often fail to accurately express the flow field structures because of the sparseness of the grid cells. Grid 3 is considered as the converged grid shape and used for subsequent numerical analysis.

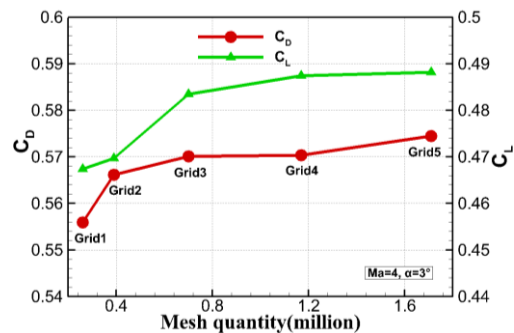


Fig. 10. Grid convergence judgment.

4.2 Flow Field Analysis

The streak images of wind tunnel tests at different angles of attack are shown in Fig. 11 while Fig. 12 shows the calculated pressure contour distributions. Comparisons of the figures show that the calculated flow field structures are in good agreement with the wind tunnel test results. The shockwaves are basically the same, which verifies that the numerical simulation method in this study has a certain accuracy and effectiveness. The surface pressure coefficient distributions demonstrate similar results for the hypersonic shockwave on the part of the nose surface by the two methods, although the computed shock wave position is much closer to surface than the experimental results, which is due to the isentropic assumption. There are some features in the experimental visualizations, such as other smaller shocks, expansion waves, and slipstreams, which are not reflected in the numerical results. This is consistent with the predicted results, as the flow field obtained by the high-speed photographic equipment used in the experiment is similar to the higher-order precision solution, while the numerical results obtained are first-order. However, the focus of the numerical calculations in this study is the macroscopic phenomenon and overall aerodynamic index. Therefore, the current

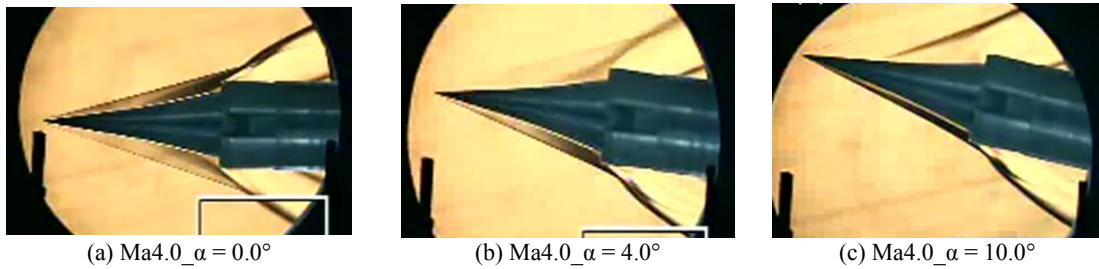


Fig. 11. Wind tunnel experiment patterns under different angles of attack.

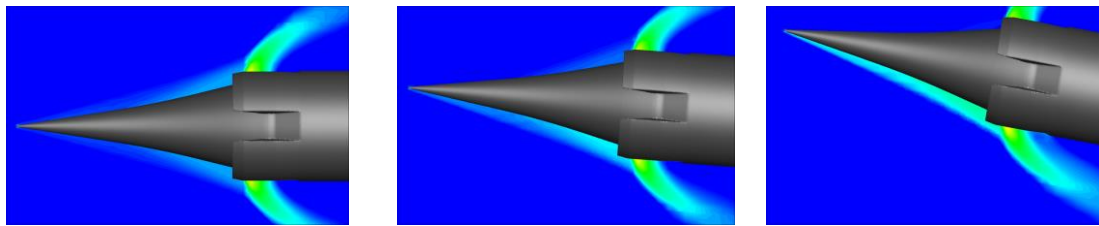


Fig. 12. The pressure contour distributions under different angles of attack.

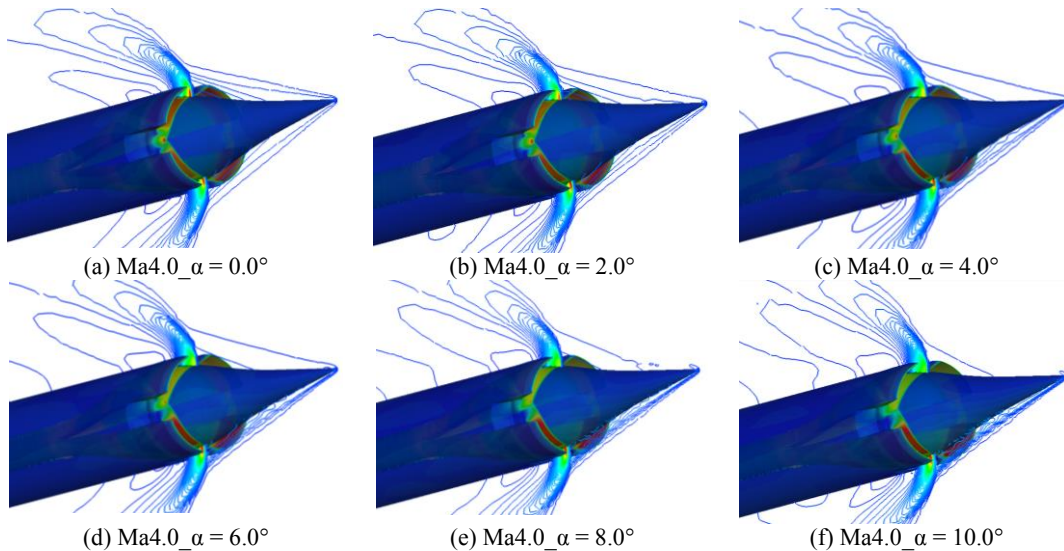


Fig. 13. Pressure contour comparison under different attack angles on the nose and inlets.

research objective has been achieved. More sophisticated calculations require more time and money. This discrepancy needs further investigation and is the subject of our future works. As a whole, the comparison indicates that the accuracy of the approach in this study is confirmed.

In order to observe the flow field structure of the air-breathing hypersonic vehicle more clearly, the pressure distribution of the aircraft head for different angles of attack is illustrated in Fig. 13. The pictures shows that the air-breathing aircraft inlets adopted four modules with 45° cross layout. When both the angle of attack and sideslip angle are zero, the pressure distributions at the lip positions of the four intake modules are the same. The strength of the shockwave at the location between two lip cowlings becomes weaker along the slice off the body, resulting in decreased pressure. The

shockwave is visible in the upwind direction and the mild shock wave in the leeward direction when the angle of attack increases, which corresponds to the pressure situation of the four inlets. Although the numerical method in this study failed to reflect the influence of laminar-to-turbulent transition in Sharma *et al.* (2018), and Chaudhuri *et al.* (2011) on aerodynamic characteristics, the main flow field wave system structure is captured. In the literature (Ding *et al.*, 2015), a similar method to solve the Euler equation was adopted to verify the applicability of the design configuration in the study of wave-rider theory.

4.3 Aerodynamic Results

The final grid was calculated for Ma = 4, and the results are compared with test data obtained in the wind tunnel. A total of ten angles of attack per train

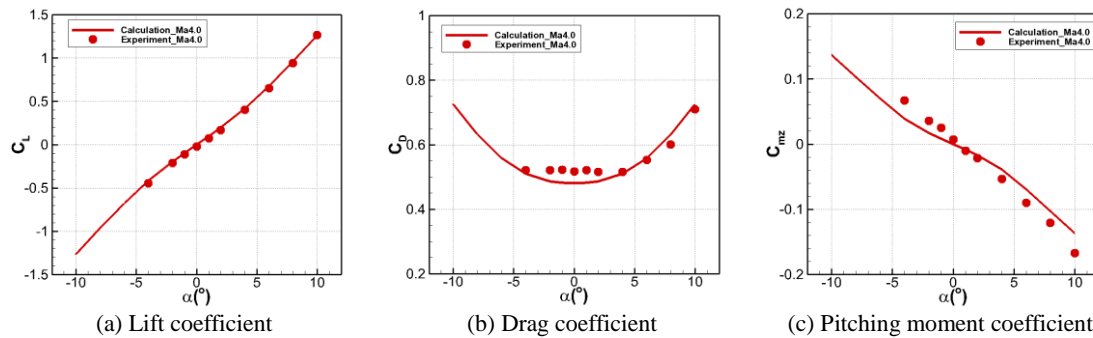


Fig. 14. Aerodynamic comparison curves between numerical results and experimental results.

were obtained in the wind tunnel test (-4° , -2° , -1° , 0° , 1° , 2° , 4° , 6° , 8° , and 10°). The calculations included more angles of attack, namely -10° , -8° , 6° , -4° , -2° , 0° , 2° , 4° , 6° , 8° , and 10° . Figure 14 shows the comparisons between the calculated results for the lift coefficient, drag coefficient, and pitch moment coefficient and the corresponding test data. The solid points represent the wind tunnel test data and the solid lines represent the numerical results.

As can be seen from the comparison curves in Fig. 14, the variable trend along the angle of attack for the calculated and test results at supersonic speeds are consistent. The calculation results of the lift coefficient agreed with the experimental data, increasing linearly within angle of attack of 10° . Figure 14(b) shows that the angle of attack is not sensitive to the experimental drag coefficient for small angles of attack ranging from -5° to 5° . A discrepancy exists between the calculated results for the drag coefficient and pitch moment coefficient and their corresponding test data, mainly because of the calculation method with in-viscid assumption. One possible reason for further analysis of the pitching moment difference is the inlet capture flow difference. The simplification of the numerical method results in increased overflow near the lip position and more obvious angle of attack effect in the windward direction. Thus, the computed pitching moment coefficient is higher than the experimental value. Taking the drag coefficient as an example, for angle of attack ranging from -10° to 10° , the maximum error is less than 7.5%, which shows the accuracy of the method in this study and its potential for applications in unconventional aircraft configuration studies. Other Mach number flight states should be further studied to enrich the conclusion on aerodynamic data deviation.

5. CONCLUSION

In this study, the developed solver and proposed meshing method are validated in the simulation for the integrated air-breathing aircraft with complex unconventional configurations. The applicability of numerical simulation method based on Cartesian grid system in the internal and external integrated flow configuration for hypersonic vehicles is studied through flow field distribution comparison

and aerodynamic data analysis. Moreover, the designed profile is developed to an experimental model for wind tunnel test. Due to the comparison results, we can conclude that under $Ma=4.0$ status, lift coefficients are consistent when the angle of attack ranges from -10° to 10° . Calculated drags have better angle of attack performance than test results as the angles of attack are small enough, such as the range between -5° and 5° . There is a difference between the pitch moment for the calculated results and their corresponding test data, however, the error is considered as acceptable because of the simplification of mathematical model in simulation and in test the flow patterns have possibility of laminar to turbulent transition. Further quantity of designs and selects for physical models could follow the simulation method as the obvious and economic advantage of high-speed, high-efficiency and a certain accuracy, especially during the aircraft conceptual design phase.

ACKNOWLEDGEMENTS

The authors are grateful for the computational resources of the Hypersonic Scramjet Technology Laboratory and portions of this research were supported by China Aerodynamics Research and Development Center (CARDC), especially the wind tunnel test.

REFERENCES

- Aftosmis, M. J., M. J. Berger and J. E. Melton (1997). Robust and efficient Cartesian mesh generation for component-based geometry. *AIAA* 1997-0196.
- Ashok, V., V. Adimurthy and G. Joseph (2014). Computation of Non-Equilibrium Chemically Reacting Hypersonic Flow from a Cartesian Mesh with Near Wall Viscous Resolution. *Journal of Applied Fluid Mechanics* 7(2),217-226.
- Chaudhuri, A., A. Hadjadj and A. Chinnayya (2011). On the use of immersed boundary methods for shock/obstacle interactions. *Journal of Computational Physics* 230, 1731-1748.

- Constant, E., J. Favier, M. Meldi, P. Meliga and E. Serre (2017). An immersed boundary method in openform: verification and validation. *Computers and Fluids* 157, 55-72.
- Dharavath, M., P. Manna and D. Chakraborty (2016). Tip-to-tail numerical simulation of a hypersonic air-breathing engine with ethylene fuel. *Acta Astronautica* 128,107-118.
- Ding, F., C. B. Shen, J. Liu and W. Huang (2015). Influence of surface pressure distribution of basic flow field on shape and performance of waverider. *Acta Astronautica* 108, 62-78.
- Huang, W. and Z. G. Wang (2009). Numerical study of attack angle characteristics for integrated hypersonic vehicle. *Applied Mathematics and Mechanics* 30, 779-786.
- Jin, L., J. Liu, S. B. Luo and Z. G. Wang (2010). Study on aerodynamic characteristics of cold flow state of hypersonic integrated aircraft. *Experimental fluid dynamics* 24(1), 42-45.
- Lakshminarayan, V. K., J. Sitaraman, B. Roget and A. M. Wissink (2017). Development and validation of a multi-strand solver for complex aerodynamic flows. *Computers and Fluids* 147, 41-62.
- Liu, Z., J. Liu, F. Ding, K. Li and Z. X. Xia (2017). Effect of thermochemical non-equilibrium on the aerodynamics of an osculating-cone waverider under different angles of attack. *Acta Astronautica* 139,288-295.
- Lockwood, M. K., D. H. Petley J. G. Martin and J. L. Hunt (1999). Airbreathing hypersonic vehicle design and analysis methods and interactions. *Progress in Aerospace Sciences* 35, 1-32.
- Lyu, F. X., T. H. Xiao and X. Q. Yu (2017). A fast and automatic full-potential finite volume solver on Cartesian grids for unconventional configurations. *Chinese Journal of Aeronautics* 30(3), 951-963.
- Piscitelli, F., L. Cutrone, G. Pezzella, P. Roncioni and M. Marini (2017). Nose-to-tail analysis of an airbreathing hypersonic vehicle using an in-house simplified tool. *Acta Astronautica* 136,148-158.
- Rong, H. J., Z. X. Yang, P. K. Wong, C. M. Vong and G. S. Zhao (2017). Self-evolving fuzzy model-based controller with online structure and parameter learning for hypersonic vehicle. *Aerospace Science and Technology* 64, 1-15.
- Shadloo, M. S. and A. Hadjadj (2017). Laminar-turbulent transition in supersonic boundary layers with surface heat transfer: A numerical study. *Numerical Heat Transfer* 72(1), 40-53.
- Shadloo, M. S., A. Hadjadj and A. Chaudhuri (2014). On the onset of post-shock flow instabilities over concave surfaces. *Physics of Fluids* 26,076101.
- Sharma, S., M. S. Shadloo and A. Hadjadj (2018). Laminar-to-turbulent transition in supersonic boundary layer: Effects of initial perturbation and wall heat transfer. *Numerical Heat Transfer, Part A: Applications* 73(9), 583-603.
- Sziroczak, D. and H. Smith (2016). A review of design issues specific to hypersonic flight vehicles. *Progress in Aerospace Sciences* 84, 1-28.
- Tang, Z. G., X. B. Xu, Y.G. Yang, X.G. Li, J. W. Dai, G. Z. Lu and W. He (2015). Technical progress of hypersonic wind tunnel aerodynamic test. *Acta Astronautica* 36(1), 86-97.
- Wang, Z. J., X. G. Li, P. Sun and X. W. Tang (2015). Design and verification of hypersonic internal outflow decoupling test system. *Propulsion technology* 36(6), 920-926.
- Wang, Z.G., X.W. Sun, W. Huang, S.B. Li and L. Yan (2016). Experiment investigation on drag and heat flux reduction in supersonic/hypersonic flows: A survey. *Acta Astronautica* 129, 95-110.
- Xu, B.Y., R.Y. Qi, B. Jiang and X. L. Yao (2017). Nussbaum gain adaptive fault tolerant control for hypersonic vehicles with uncertain parameters and actuator faults. International Federation of Automatic Control, Hosting by Elsevier Ltd.
- Xu, C., Y. W. Wang, C. G. Huang, C. Yu and J. Huang (2018). Analysis of Near-wall effect on cloud cavitating flow that surrounds an axisymmetric projectile using large eddy simulation with Cartesian cut-cell mesh method. *European Journal of Mechanics /B Fluids* 67, 15-24.
- Yelan, L., B. Yang and Z. Peng(2015). Patent analysis of the course of aerojet's business and the key technologies of hypersonic. *Procedia Engineering* 99, 773-779.
- Yentsch, R. J. and D.V. Gaitonde (2013). Numerical Investigation of the HIFiRE-2 Scramjet Flowpath. 51st AIAA Aerospace Sciences Meeting.